

# Numerical study on RC and HPFRCC slabs exposed to TNT explosion near ground

MinJoo Lee<sup>1a</sup>, Hyo-Gyoung Kwak<sup>1b</sup>, Sung-Wook Kim<sup>2c</sup> and Gang-Kyu Park<sup>\*2</sup>

<sup>1</sup>Department of Civil and Environmental Engineering, KAIST, Daejeon 34141, Republic of Korea

<sup>2</sup>Department of Structural Engineering Research, Korea Institute of Civil Engineering and Building Technology, 283 Goyangdae-Ro, Ilsanseo-Gu, Goyang-Si 10223, Korea

(Received March 27, 2023, Revised May 24, 2023, Accepted May 25, 2023)

**Abstract.** In this paper, the structural performance of RC and HPFRCC slabs exposed to a TNT explosion were numerically investigated. A finite element model was established using the MM-ALE method in the LS-DYNA program to simulate a near-ground TNT explosion at a scaled distance of 1.08 m/kg<sup>3</sup>. The K&C model was calibrated to exactly reflect the material properties of HPFRCCs that were developed in KICT and KNU. Numerical and experimental results were compared for the damage distribution and failure shape of the slabs. Based on the verified numerical model, a parametric study was carried out to demonstrate the effects of compressive strength and thickness of the slab on the blast resistance. In particular, the spallation failure on the back side of the slab is greatly dependent on the thickness. Finally, additional numerical simulations were conducted to explore the variation in blast pressure characteristics according to the scaled distance and explosive shape. It was confirmed that the pressure induced by cubic TNT was more destructive to the slab than cylindrical and spherical TNT in a near-field explosion.

**Keywords:** ALE method; HPFRCC; parametric study; TNT explosion

## 1. Introduction

With growing concerns about explosions and bombing attacks, improving the blast-resistance capacity has become one of the most important factors in terms of the safety of concrete structures. Considering the design of a structure, it is the strain rate effect that distinguishes the structural behavior under blast loading conditions compared to static loading conditions. This is due to an increase in the material properties with a viscous effect, evolution of the cracks, and inertial force effect under very high amplitude loading with short duration (Cui *et al.* 2017). It is therefore necessary to carefully consider the strain rate effect on the constituent materials in concrete-based structures subjected to blast loadings.

When concrete structures are subjected to an explosion, abundant debris and fragments are generated on the rear side due to the brittle characteristic of concrete, which can lead to secondary damage inside the protective facility including the loss of human life. Among various approaches developed to address this problem, high-performance fiber-

reinforced cement composites (HPFRCCs) have been reported to show good resistance capacity against extreme loadings as they have a higher matrix strength due to their dense internal microstructure, energy absorption, and ductility owing to a bridging effect between cracks (Tufekci and Gokce 2017, Yoo *et al.* 2017). In addition, the use of externally bonded basalt fiber reinforced polymer (BFRP) sheets is known to be a good option to improve the energy absorption capacity, ductility, and the resistance to fragmentation, with advantages of low cost and corrosion resistance (Dhand *et al.* 2015, Chen *et al.* 2018, Li *et al.* 2017). Given that the introduction of HPFRCCs and FRP strengthening has a strong influence on the structural behavior, various studies have been conducted on specimens to which HPFRCC and FRP sheets are applied (Chen *et al.* 2020, Baggio *et al.* 2014, Ren *et al.* 2018, Kim *et al.* 2022), ranging from research on static and dynamic mechanical characteristics to evaluations of the resistance capacity of the structures under extreme loading conditions.

Kim *et al.* (2022) manufactured HPFRCC specimens by combining long steel fibers and long nylon fibers. Contact detonation and military land mine explosive tests using TNT were carried out on these specimens, and maximum damage depth and mass change rate after the experiments were measured. It was reported that using only nylon fibers did not provide proper protection resistance capability, whereas the specimens using long steel fibers and nylon fibers together showed better resistance performance against the explosion than those using only long steel fibers. Kumar *et al.* (2020) performed blast experiments using gelatin explosive on reinforced concrete slabs, and the influences of different quantities of the explosive and

\*Corresponding author, Postdoctoral Researcher

E-mail: gkpark@kict.re.kr

<sup>a</sup>Postdoctoral Researcher

E-mail: minjoolee1212@kaist.ac.kr

<sup>b</sup>Professor

E-mail: kwakhg@kaist.ac.kr

<sup>c</sup>Senior Research Fellow

E-mail: swkim@kict.re.kr

standoff distance on the failure modes and damage level of the slabs were investigated. One-way bending and subsequent splitting of the slab became dominant as the explosive charge was increased. The failure mode of the specimens gradually changed from localized failure to globalized bending behavior as the standoff distance increased. Xu *et al.* (2016) conducted a series of field blast tests on high strength reinforced concrete (HSRC) and ultra-high performance fiber reinforced concrete (UHPFRC) columns to investigate their structural behavior under the same loading condition. The level of damage and permanent deflections of each specimen were compared, and it was observed that UHPFRC afforded superior performance in terms of explosion resistance over HSRC. It was also confirmed that the specimen subjected to axial loading showed smaller deflection due to the limitation of the end rotation. Chen *et al.* (2020) manufactured RC slabs strengthened by BFRP strips with various strengthening layout schemes. The impact resistance to drop hammer tests was investigated to identify the failure modes and to measure the indentation depth and area. It was observed that the use of BFRP sheets on the back side of the slabs is considerably effective in improving the impact resistance capacity and mitigating damage accumulation and crack development. Among various types of layouts, placing BFRP strips at an angle of  $\pm 45^\circ$  was found to offer the best performance in restraining crack development. It was also found that the structural behavior of RC slabs changed from global flexural failure to a local punching shear failure as the impact energy increased.

Due to spatial and financial limitations, it is difficult to perform various explosion tests, and thus various numerical studies have been actively carried out based on available experimental results. Su *et al.* (2021) carried out numerical simulations using the CONWEP method embedded in the LS-DYNA for free air blast tests on ultra-high performance concrete (UHPC) and normal concrete (NC) panels. The numerical models were verified by comparing the overpressure, deflection, and damage distribution of experimental results, and the applicability of CONWEP was demonstrated under a specific scaled distance range. However, they also revealed the limitations of CONWEP in describing the charge shape and detonation point, which become increasingly prominent as the scaled distance decreased. Liu *et al.* (2022) introduced a calibration method of the Karagozian and Case (K&C) concrete model to reflect the material properties of UHPC in numerical analyses. The validity of the numerical model using the ALE formulation was assessed by comparing the failure modes, crater, and scabbing damage with experimental results. A parametric study was also conducted and an empirical equation was thereupon proposed to predict the local damage mode of concrete structures according to slab thickness and scaled standoff distance. Luccioni *et al.* (2018) established finite element models using the Euler Lagrange interaction coupling option embedded in the AUTODYN for simulating a contact explosion. Numerical analyses were performed for high-strength fiber reinforced concrete (HSFRC) slabs with different types and contents of hooked-end steel fibers, including plain concrete slabs. The results revealed that it is not easy to describe the structural

behavior of HSFRC based on the calibrated material model due to insufficient available test data. It was also observed that the same erosion value cannot be used for the HSFRC specimens because the flexural strength and resisting capacity are highly dependent on the type and contents of steel fibers.

Although several studies on explosion tests and simulations have been presented, there has been limited research where the material model has been calibrated properly and TNT explosion tests have been carried out for HPFRCC and BFRP-retrofitted structures. In addition, while there have been many numerical studies on close-range or contact explosions that cause localized damage owing to the relatively large number of experiments reported in previous literatures, numerical approaches for TNT explosion at long standoff distances with a considerable amount of TNT to evaluate the overall structural behavior and resisting capacity are quite limited due to the small number of relevant experiments that have been conducted. In this study, numerical analyses are conducted on the experimental results of an explosion test with 100 kg of TNT on cement-based structures, conducted by Korea Institute of Civil Engineering and Building Technology (KICT) (Korea Institute of Civil Engineering and Building Technology (KICT) 2017) and Kangwon National University (KNU) (Jung *et al.* 2017). Two different HPFRCC slabs were considered with an RC slab. KICT-HPFRCC is a cement-based material reinforced only with steel fibers, while KNU-HPFRCC is a material reinforced with steel fibers as well as BFRP sheets on the exterior. The structural performance according to the internal and external reinforcement methods was compared.

This study is organized as follows: Section 2 explains the experimental setup for the TNT explosion. Section 3 briefly introduces the calibration method of the K&C model for HPFRCCs, and verifies the calibrated model through a static analysis of a four-point bending test. Section 3 In Section 4, finite element numerical models using the Multi-Materials Arbitrary Lagrangian-Eulerian (MM-ALE) are established for plain concrete, and HPFRCC slabs among the specimens subjected to blast loading in the KICT report (Korea Institute of Civil Engineering and Building Technology (KICT) 2017). Section 5 presents a comparison between experimental and numerical results. Moreover, blast pressures calculated from the established numerical model are compared with those obtained from the Load Blast Enhanced (LBE) method. In Section 6, parametric studies for variations in matrix strength and specimen thickness are conducted to examine which parameter is more dominant for effective protection design. Additional numerical analyses are performed to investigate the differences between the explosive characteristics and failure shape of the specimens according to the modeling shapes of TNT explosive and scaled distance. Conclusions are given in Section 7.

## 2. Experimental program

TNT explosion tests were conducted by KICT and KNU to examine the blast-resistant performance of the developed

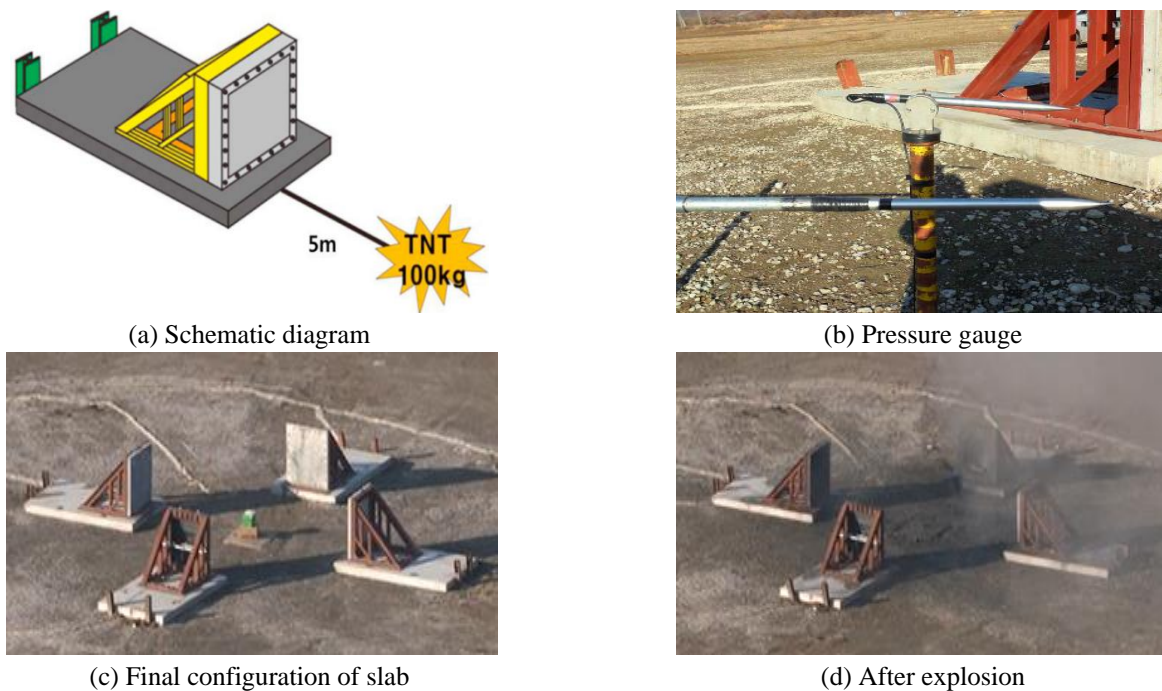


Fig. 1 TNT explosion test setup (Korea Institute of Civil Engineering and Building Technology (KICT) 2017)

HPFRCCs (Jung *et al.* 2017, Korea Institute of Civil Engineering and Building Technology (KICT) 2017). KICT-HPFRCC is a cement based composite reinforced by straight steel fibers of 2.0% with a diameter of 0.2 mm and a length of 19.5 mm, and it had a designed compressive strength of 180 MPa. Details of the material properties for KICT-HPFRCC can be found in (Lee *et al.* 2021, Korea Institute of Civil Engineering and Building Technology (KICT) 2017). KNU-HPFRCC with a compressive strength of 80 MPa is a SIFCON (slurry infiltrated concrete) based HPFRCC reinforced by steel fibers of 5.0% with a diameter of 0.75 mm and a length of 60 mm, and it is externally wrapped by BFRP sheet. The BFRP sheet has a tensile strength of 1,688 MPa and an elastic modulus of 80.4 MPa (Korea Institute of Civil Engineering and Building Technology (KICT) 2017). Normal concrete (NC) with a compressive strength of 25 MPa was used as a control specimen for comparison. All targets have dimensions of 1.9 m×1.9 m×0.105 m, and SD400 reinforcing bars with a diameter of 10 mm and yield strength of 400 MPa were used. The spacing of the reinforcing bars was set to 240 mm both vertically and horizontally.

In the test, TNT with a mass of 100 kg was employed and the standoff distance from the slab was 5 m. A schematic diagram of the TNT experiment is shown in Fig. 1(a). The target slabs are placed on heavy concrete bases to prevent the slabs from being displaced by the blast pressure. All four sides of the slab were bolted to the steel frame. In order to prevent measurement error due to complete destruction of structural members, the pressure gauge was installed at the same distance from the TNT as the slab (see Fig. 1(b)). Thus, the incident pressure was measured instead of the reflected pressure. The TNT explosive has a cubic shape. In order to reduce the cost of the field test, a total of four slabs including a slab from another institution were

tested, and these slabs are located at the same distance from the TNT explosive (see Fig. 1(c)). The TNT was placed slightly off the ground as it was located on top of a wooden box. A high-speed camera was installed at a sufficient distance from the test place to ensure safety to capture the process of the explosion, as seen in Fig. 1(d).

### 3. Constitutive material models

HPFRCCs reinforced by steel fibers have improved material properties such as high compressive strength, tensile strength, and toughness. KICT and KNU used different fiber aspect ratios, fiber contents, and matrix strengths when manufacturing HPFRCC specimens. Thus, the material model should reflect the difference in material properties due to the mix design. In this study, the K&C model was adopted to consider the mechanical characteristics of the HPFRCCs. The K&C model is basically composed of deviatoric and volumetric components. The model parameters for three failure strength envelopes, damage function, and damage evolution parameters is responsible for the deviatoric response, and the equation of state (EOS) is used to consider the volumetric strain-pressure relationship. The model can also account for strain rate sensitivity by defining the strain rate-dynamic increase factor (DIF) curve for both compression and tension. The reliability of the calibrated K&C model and its applicability to ballistic impact simulation for HPFRCCs were verified in previous studies (Lee *et al.* 2022, 2021). In this study, the model parameters in the K&C model for the two types of HPFRCCs were modified based on the calibration method proposed by Lee *et al.* (2021), where a detailed description of the calibration procedure can be found. Meanwhile, in the case of the RC

Table 1 Material parameters of for KICT-HPFRCC (units: m, Pa, s)

Parameter	Value	Parameter	Value	Parameter	Value	Parameter	Value
$a_0$	6.670E+7	$b_2$	-2.0	$\lambda_9$	0.001	$\eta_5$	1.0
$a_1$	0.4907	$\lambda_1$	0.0	$\lambda_{10}$	0.002	$\eta_6$	0.842
$a_2$	2.860E-10	$\lambda_2$	2.800E-5	$\lambda_{11}$	0.004	$\eta_7$	0.684
$a_{0y}$	5.555E+7	$\lambda_3$	8.000E-5	$\lambda_{12}$	0.008	$\eta_8$	0.478
$a_{1y}$	0.7905	$\lambda_4$	1.400E-4	$\lambda_{13}$	1.0E+10	$\eta_9$	0.184
$a_{2y}$	7.470E-10	$\lambda_5$	2.415E-4	$\eta_1$	0.0	$\eta_{10}$	0.097
$a_{1f}$	0.4669	$\lambda_6$	3.000E-4	$\eta_2$	0.218	$\eta_{11}$	0.056
$a_{2f}$	2.790E-10	$\lambda_7$	3.500E-4	$\eta_3$	0.553	$\eta_{12}$	0.033
$b_1$	1.0	$\lambda_8$	4.500E-4	$\eta_4$	0.823	$\eta_{13}$	0.0

Table 2 Material parameters for KNU-HPFRCC (units: m, Pa, s)

Parameter	Value	Parameter	Value	Parameter	Value	Parameter	Value
$a_0$	2.747E+7	$b_2$	1.0	$\lambda_9$	0.001	$\eta_5$	1.0
$a_1$	0.4907	$\lambda_1$	0.0	$\lambda_{10}$	0.002	$\eta_6$	0.801
$a_2$	6.940E-10	$\lambda_2$	2.800E-5	$\lambda_{11}$	0.004	$\eta_7$	0.717
$a_{0y}$	2.884E+7	$\lambda_3$	2.000E-4	$\lambda_{12}$	0.008	$\eta_8$	0.652
$a_{1y}$	0.7905	$\lambda_4$	3.400E-4	$\lambda_{13}$	1.0E+10	$\eta_9$	0.640
$a_{2y}$	1.814E-9	$\lambda_5$	4.180E-4	$\eta_1$	0.0	$\eta_{10}$	0.532
$a_{1f}$	0.4669	$\lambda_6$	6.000E-4	$\eta_2$	0.130	$\eta_{11}$	0.464
$a_{2f}$	6.780E-10	$\lambda_7$	7.500E-4	$\eta_3$	0.728	$\eta_{12}$	0.356
$b_1$	1.0	$\lambda_8$	9.500E-4	$\eta_4$	0.965	$\eta_{13}$	0.0

slab, parameters of the K&C model were automatically generated with a given compressive strength.

The material parameters for the failure strength envelopes are calculated depending on uni- and multi-axial strength tests, and the three failure strengths are expressed in Eq. (1) (Lee *et al.* 2021). The damage function parameters are obtained according to the compressive strength, steel fiber volume fraction, and aspect ratio, as described in (Lee *et al.* 2021). The damage evolution parameters (or softening parameters) were determined by an iterative procedure through comparison with the material test results. Accordingly, the material parameters for KICT-HPFRCC and KNU-HPFRCC are summarized in Table 1 and Table 2. The EOS card in LS-DYNA defines the volumetric strain-pressure curve and the corresponding bulk modulus, and the values suggested by Su *et al.* (Su *et al.* 2021) were used in this paper.

$$a_0=0.34339f_c \quad a_1=0.49067 \quad a_2=0.05554/f_c \quad (1a)$$

$$a_{0y}=0.28606f_c \quad a_{1y}=0.79045 \quad a_{2y}=0.14515/f_c \quad (1b)$$

$$a_{0f}=0 \quad a_{1f}=0.4669 \quad a_{2f}=0.05421/f_c \quad (1c)$$

In order to verify the constitutive models for the HPFRCCs, numerical analyses of a four-point bending test were carried out. This study adopted experimental results from (Korea Institute of Civil Engineering and Building Technology (KICT) 2017) where a beam specimen of 0.1 m×0.1 m×0.4 m was tested in accordance with KS F 2566 (KS F 2566 2014). The effective span length of the

specimen between bottom supports was 0.3 m, and a simply supported condition was assumed as the boundary condition. Two force rollers were applied to the top of the specimen, which were spaced 0.05 m apart from the center to the left and right, respectively. The numerical model for four-point bending was set up using solid elements, as shown in Fig. 2(a). The load-displacement curves obtained from the numerical simulation were compared with those from the test. As shown in Fig. 2(b), the numerical results show good agreement with the experiment, thus demonstrating that the material properties of the HPFRCCs are properly considered in the K&C model. Although the maximum load applied to the KICT-HPFRCC beam is larger than that applied to the KNU-HPFRCC beam, the KNU-HPFRCC showed better energy absorption capacity in the softening area than the KICT-HPFRCC.

The strain rate sensitivity of the material properties for HPFRCCs must be considered in the analysis of extreme loading conditions such as in the case of a TNT explosion. The DIF equations suggested by Lee *et al.* (2021) and Park *et al.* (2017) were adopted in this paper for compression and tension, respectively. The input parameters for the strain rate and DIF values are summarized in Table 3. In this relationship, negative values of the strain rate represent the tensile behavior and positive values represent the compressive behavior. The strain rate-DIF relation can be directly applied to the K&C model. Moreover, cut-off values of DIFs should be taken into account, according to a previous work (Lu *et al.* 2017, Cui *et al.* 2017), to exclude the overestimated DIF due to the inertia effect at a high

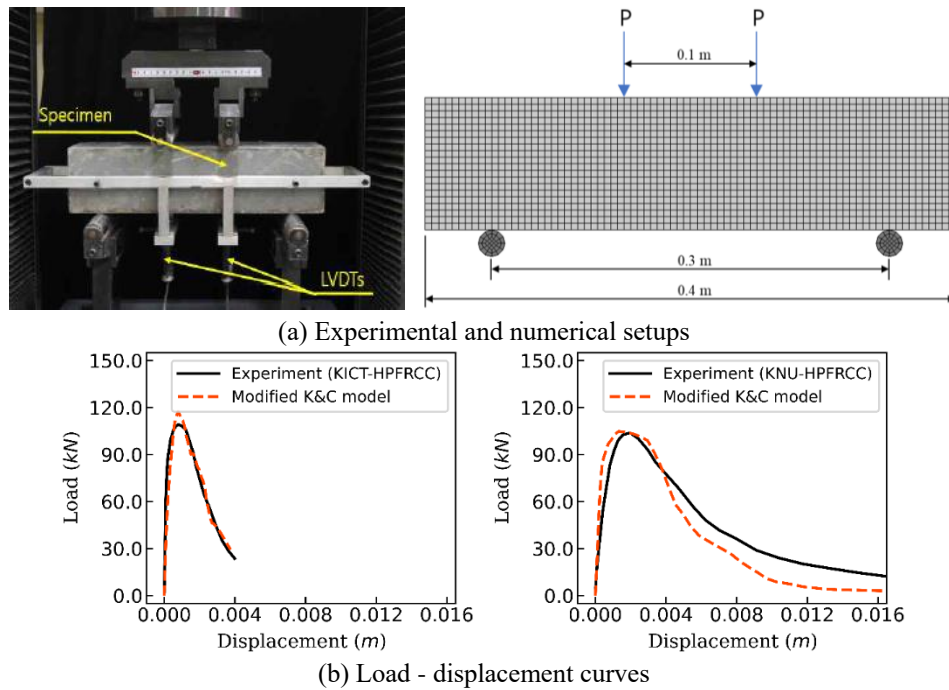


Fig. 2 Numerical setup and results for four-point bending test

Table 3 DIF values used in K&C model

Strain rate (1/s)	DIF value	Strain rate (1/s)	DIF value	Strain rate (1/s)	DIF value
1000.0	2.288	0.01	1.085	-1.0	1.265
500.0	2.288	0.001	1.050	-3.0	1.289
300.0	2.288	0.0001	1.017	-25.0	1.336
50.0	1.222	0.0	1.000	-30.0	1.479
25.0	1.210	-0.0001	1.081	-53.0	1.934
3.0	1.175	-0.001	1.125	-300.0	4.380
1.0	1.157	-0.01	1.169	-1000.0	4.380

strain rate. Therefore, the cut-off values were determined at DIF values of 300/s for compression and 100/s for tension, as recommended in a previous study (Zhang *et al.* 2021).

In addition, the BFRP sheet has high tensile properties, but its performance depends on the attached direction. In this case, BFRP sheets with a relatively thin thickness have an orthotropic property. Thus, \*Mat\_Enhanced\_Composite\_Damage model was used as the material model for the BFRP sheet. The BFRP sheet shows linear elastic behavior as the stress reaches the tensile strength. Failure occurs without softening behavior after reaching the tensile strength. Material properties not mentioned in the experiment were assumed.

#### 4. Numerical simulation using MM-ALE method

Numerical simulations for the TNT explosion can be performed by the LBE method or the MM-ALE method in the LS-DYNA program. The LBE method adopts an empirical equation to describe the blast pressure-time profile according to the type of blast source such as a

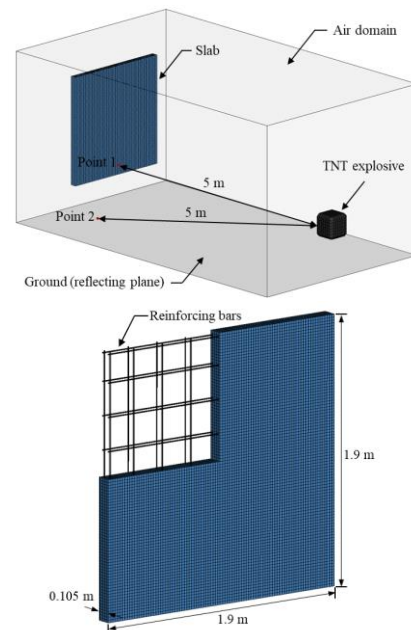
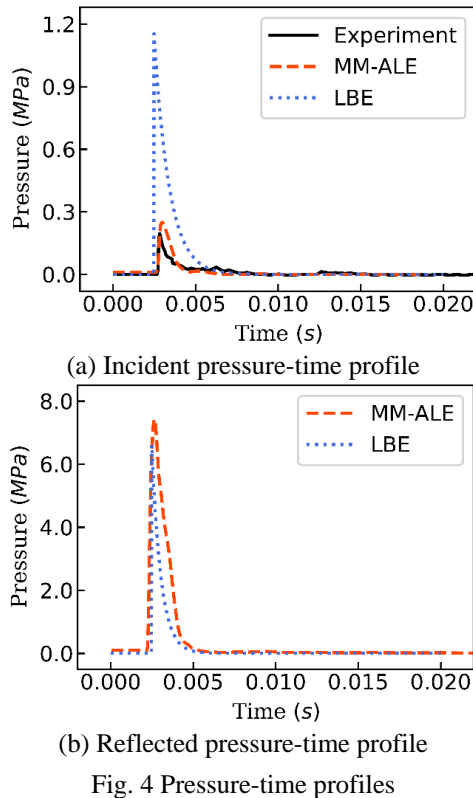


Fig. 3 Numerical setup using MM-ALE method and slab details for the TNT explosion test

spherical blast burst and hemispherical blast burst. On the other hand, the MM-ALE method simulates the blast wave propagation through modeling of the TNT and air by Eulerian solid elements and a structure by Lagrangian solid elements, which enables the fluid-structure interaction. Therefore, the MM-ALE method is more appropriate for exactly simulating complicated loading conditions, considering explosive shapes and ground reflection. Thus, in this paper, a numerical model was established using the MM-ALE method. As shown in Fig. 3, a target slab was modeled by Lagrangian elements with a size of 10 mm and



all sides of the slab are fully fixed. The TNT explosive and air domain were modeled by Eulerian elements. The BFRP sheet attached to the HPFRCC slab was modeled by shell elements. The TNT explosive has a cubic shape, as applied in the experiment. An air domain with a mesh size of 10 mm surrounded the TNT explosive and slab, and the ground face in the air domain was considered as a reflecting plane and the remaining planes were set to non-reflecting planes. Both the incident and reflected pressures were measured by \*Database\_Tracer at points 1 and 2, respectively (see Fig. 3). Point 1 was located on the slab. Point 2 was located 5 m away from the TNT, and was unaffected by reflected pressure of the slab.

## 5. Experimental and numerical results

In order to demonstrate the accuracy of the MM-ALE method, the incident pressure-time profiles obtained from both the MM-ALE and LBE methods are compared with that obtained from the pressure gauge in the explosion test. In the case of the LBE method, the blast type was set to a hemispherical blast burst and the shape of the TNT explosive was spherical, which is the only option for the LBE method. As shown in Fig. 4, the maximum incident pressure of 0.24 MPa obtained from the MM-ALE provides a good approximation to the experimental value of 0.2 MPa. On the other hand, that of the LBE method assuming a hemi-spherical surface burst is 1.15 MPa (see Fig. 4(a)), which deviates significantly from the experimental result. Nevertheless, the reflected pressures applied on the slab from the MM-ALE and LBE methods are similar, as shown

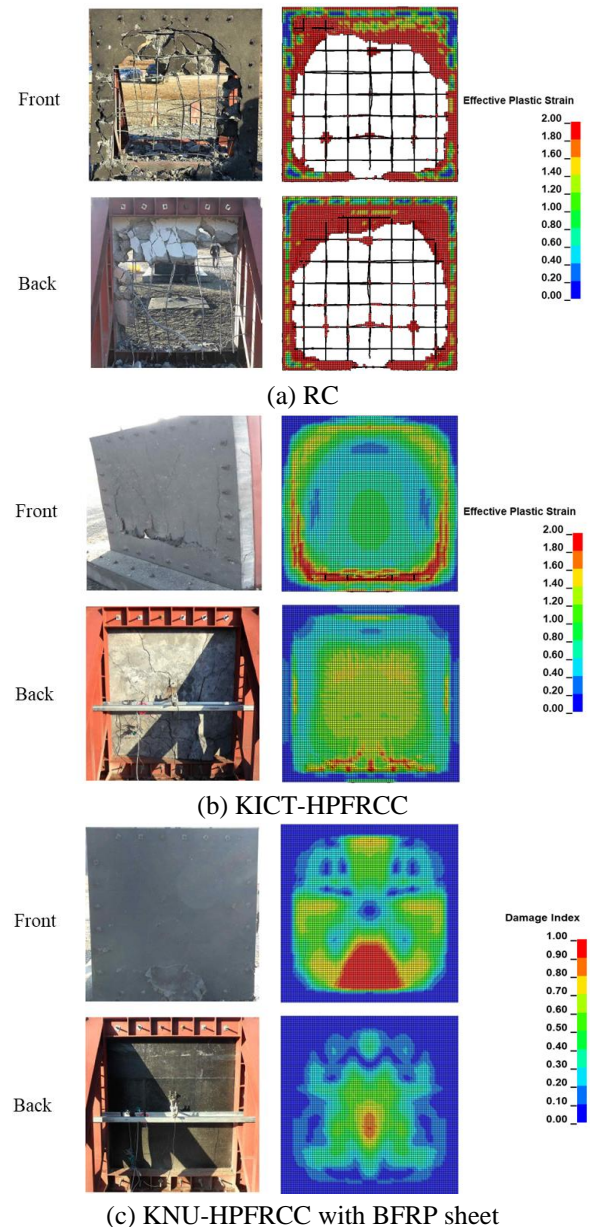


Fig. 5 Failure mode and damage distribution of RC/HPFRCC slabs for TNT explosion

in Fig. 4(b), at approximately 7 MPa. In general, high incident pressure leads to high reflected pressure, but the numerical results from the LBE method do not follow this tendency. Since the LBE method is based on empirical equations, the influences of the TNT geometry and the size and shape of the structure subjected to blast load are not carefully accounted for in the numerical analysis. Therefore, while the LBE method may give high accuracy in the spherical free-air burst that occurred at long distance from the target, it appears to be difficult to achieve numerical reliability when complex explosion phenomena occur as the scaled distance becomes smaller, or when the shape of the explosive is not spherical.

Fig. 5(a) shows the failure mode and damage distribution of the slabs for the TNT explosion. It can be observed that the numerical results provide reasonable

Table 4 Results of parametric study

Case	Compressive strength (MPa)	Thickness (mm)	Displacement (mm)	Failure mode
1	100	105	19.6	no spallation
2	140	105	18.2	no spallation
3	180	105	17.5	no spallation
4	180	94.5	23.6	no spallation
5	180	84	37	no spallation
6	180	73.5	101	spallation on the back side
7	180	63	175	spallation on the back side

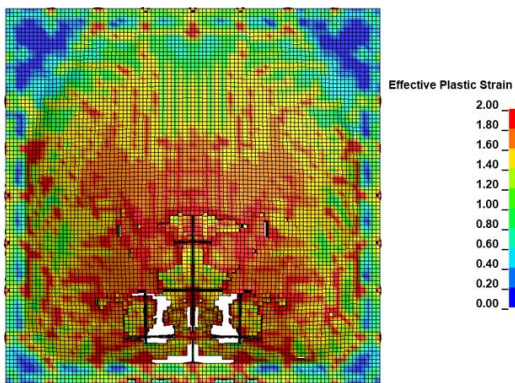


Fig. 6 Failure mode on the back side of the slab with thickness of 63 mm

agreement with the experiments for all specimens. The RC slab was completely destroyed and the reinforcing bars were severely deformed or disconnected. The TNT burst at a location lower than the center of the slab, causing significant damage to the lower part of the slab, including the concrete region anchored to the steel frame. On the other hand, in the HPFRCCs reinforced by steel fibers, there was a considerable reduction in damage compared to the RC slab. Although the KICT-HPFRCC slab underwent damage at low height near the boundary, it is expected that it would maintain its structural performance (see Fig. 5(b)). In addition, the KNU-HPFRCC slab with BFRP sheet received the smallest amount of damage among the test specimens despite having a relatively low compressive strength of 80 MPa. As shown in Fig. 5(c), both the experiment and the numerical simulation showed damage on the front side of the BFRP sheet. It is found that a high content of steel fibers in the cement matrix and the BFRP sheet reinforcement play an important role in the blast-resistance. However, it is noted that it is difficult to achieve reliable performance due to the mix uncertainty when reinforcing high-content steel fibers in cement materials.

The displacement-time curve also was measured in the experiment. However, the base where the target specimen was fixed was pushed out by the blast pressure and the contact between LVDT and the specimen was lost, and it appears that these factors would affect the measurement of the displacement. Therefore, in this paper, the

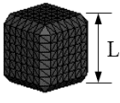
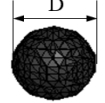
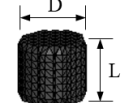
displacements of the specimens obtained from the test were not compared with the numerical results.

## 6. Parametric studies

Since the spallation on the back side due to the shock wave is a major cause of potential injury and loss of life and affects the structural integrity and stability of concrete structures, a protective design that prevents spallation failure is essential. Based on the validated numerical model, as shown in the previous section, compressive strength and specimen thickness were selected as parameters that greatly affect the failure mode related to structural performance. Three different compressive strengths (100 MPa, 140 MPa, 180 MPa) developed in a previous study (Korea Institute of Civil Engineering and Building Technology (KICT) 2017), and four different thicknesses (94.5 mm, 84 mm, 73.5 mm, 63 mm) were considered. The central displacements and failure modes of the slabs were measured and compared according to the parameters. The input variables in the K&C model were calibrated based on the mechanical properties of HPFRCCs reinforced with 2% steel fibers in a previous study (Lee *et al.* 2022) according to the procedure proposed in Lee *et al.* (2021). Table 4 summarizes the displacement and failure mode of each case obtained through the numerical analyses. The results from Case 1 to Case 3 show that as the compressive strength decreases by about 40%, from 180 MPa to 100 MPa, the displacement increases by 12%. Nevertheless, none of the three specimens suffered from spallation failure on the back side. As the blast wave passes through the thickness of the specimen and reaches the back of the specimen as a tensile wave, the tensile strengths for Cases 1-3 appear to be large enough to resist the tensile wave. On the other hand, it can be seen in Table 4 that the structural performance degrades rapidly with decreasing thickness. In the case of the specimen with a thickness of 63 mm, a 40% reduction from 105 mm thickness, a large permanent deformation occurred and the safety of the structure could not be guaranteed (see Fig. 6). It was found that the magnitude of the arriving tensile waves decreases greatly as the thickness increases. The parametric study confirmed that the reduction in thickness has more effect on the structural performance than the reduction of compressive strength. Thus, a compressive strength of 100 MPa or more is sufficient to withstand a TNT explosion, but a slab design with a minimum thickness of 84 mm is required to meet the protective performance.

UFC 3-340-02, an explosive safety manual, considers spherical or hemispherical detonation by spherical explosives and the empirical equation to evaluate the blast pressure is expressed as a function of the scaled distance and incident angle (DOD 2008). However, the magnitude and direction of the blast wave propagation highly depend on the explosive shape in the near-field explosion. Thus, numerical simulations for different shapes of the TNT explosive, that is, spherical and cylindrical shapes, were performed using the MM-ALE method to understand how the explosive shape affects the propagation and magnitude of blast pressure and the structural behavior in the

Table 5 Details of the explosive types and geometry

Type	Cube	Sphere	Cylinder
Geometry			
	$L = 0.3944$	$D = 0.4892$	$D = 0.445, L = 0.3944$

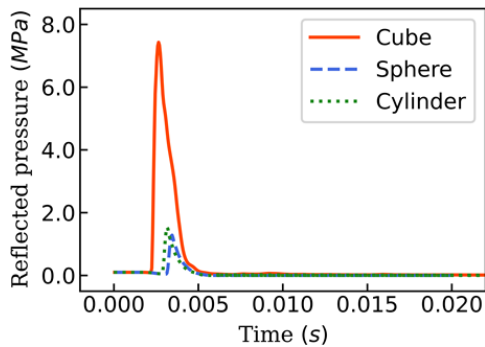
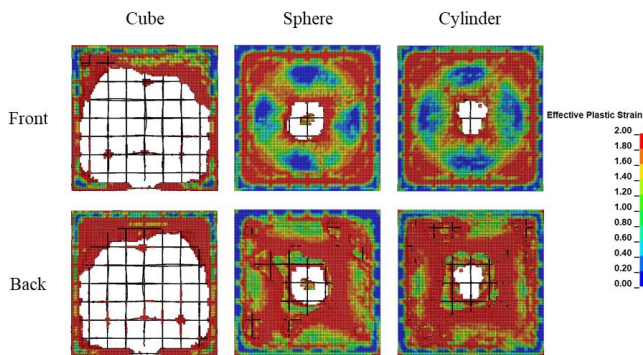
Fig. 7 Reflected pressure - time profiles according to the explosive type at scaled distance of  $1.08 \text{ m/kg}^3$ 

Fig. 8 Fracture shapes of the RC slab according to the explosive type

simulation. The explosives considered have the same mass as the cubic explosive, and the geometric details of each explosive are presented in Table 5. The ratio of length to diameter ( $L/D$ ) for the cylindrical explosive is about 0.886. The axial direction of the cylindrical explosive was positioned parallel to the slab, and the blast wave propagated to the slab in the radial direction of the cylindrical explosive. The explosive is located 5 m from the normal concrete slab, as in the previous section. As shown in Fig. 7, the reflected pressure-time profiles according to the explosive type are compared. The maximum reflected pressure induced by the cubic explosive was much larger than those induced by other explosives, and there was a difference in the arrival time of the blast wave to the slab. Fig. 8 shows the fracture shapes and plastic damage distributions of the target slabs caused by three different explosives. The spherical and cylindrical explosives lead to small local damage at the center of the slab compared to the cubic explosive, but overall plastic damage is observed on both sides of the slab.

The difference in the reflected pressure appears to be related to the propagation characteristics of the blast wave.

In previous studies, it was noted that the blast wave of spherical explosives propagates uniformly in all directions, while for other types of explosives the propagation magnitude and the speed of the blast wave depend on the explosive geometry and orientation (Shi *et al.* 2022, Gan *et al.* 2023, Wu *et al.* 2010). These characteristics according to the explosive shape can be seen in Fig. 9. At the beginning of the explosion, the direction of the blast wave was affected by the shape of the explosive. As propagation proceeds, the magnitude and speed of the blast wave increased near the ground due to the ground reflection effect, and the difference according to the explosive type was also enlarged. In particular, it was found that the cubic explosive produces a larger and faster blast pressure wave than the other explosives, which leads to considerable damage to the specimen (see Fig. 8).

Fig. 10 presents the maximum reflected pressure and arrival time with the scaled distances according to the shape of the TNT explosive. The scaled distances were calculated for the 100 kg TNT at five stand-off distances (5 m, 6 m, 7 m, 8 m, and 9 m). As shown in Fig. 10, the maximum reflected pressure considerably decreased as the scaled distance increased. It also can be found that the effect of the TNT geometry on the reflected pressure diminished with an increase in the scaled distance. Moreover, the influence of the TNT geometry on the time for the blast pressure to reach the slab increased as the scaled distance increased. It is observed that the numerical tendency for the cubic TNT explosive are gradually different from those of the other explosives according to the scaled distance. In particular, the cylindrical explosive shows similar reflected pressure to the spherical explosive at the small scaled distance. The reflected pressure for cylindrical explosives highly depends on the orientations of the explosives for pressure measurement (e.g., radial and axial directions) and the value of  $L/D$  (Wu *et al.* 2010). The radial orientation and a small value of  $L/D$  appear to induce relatively small pressure (see Fig. 10).

## 7. Conclusions

This paper numerically investigated the performance of RC, KICT-HPFRCC, and KNU-HPFRCC with BFRP sheet slabs under a near-ground TNT explosion. The numerical model for the TNT explosion using the MM-ALE method was verified through a comparison with the test results. Furthermore, numerical simulations were performed to investigate the effects of the compressive strength and thickness on the structural performance of the slabs as well as the blast wave propagation properties according to the explosive shape. The conclusions are as follows:

- (1) The accuracy of the simulation for incident and reflected blast pressures was improved by using the MM-ALE method, which can model the air domain and TNT as Eulerian elements. Input parameters of the K&C model were calibrated to reflect the improvement on the material properties of HPFRCCs, which were manufactured by KICT and KNU, respectively. The modified K&C model was verified by a static analysis

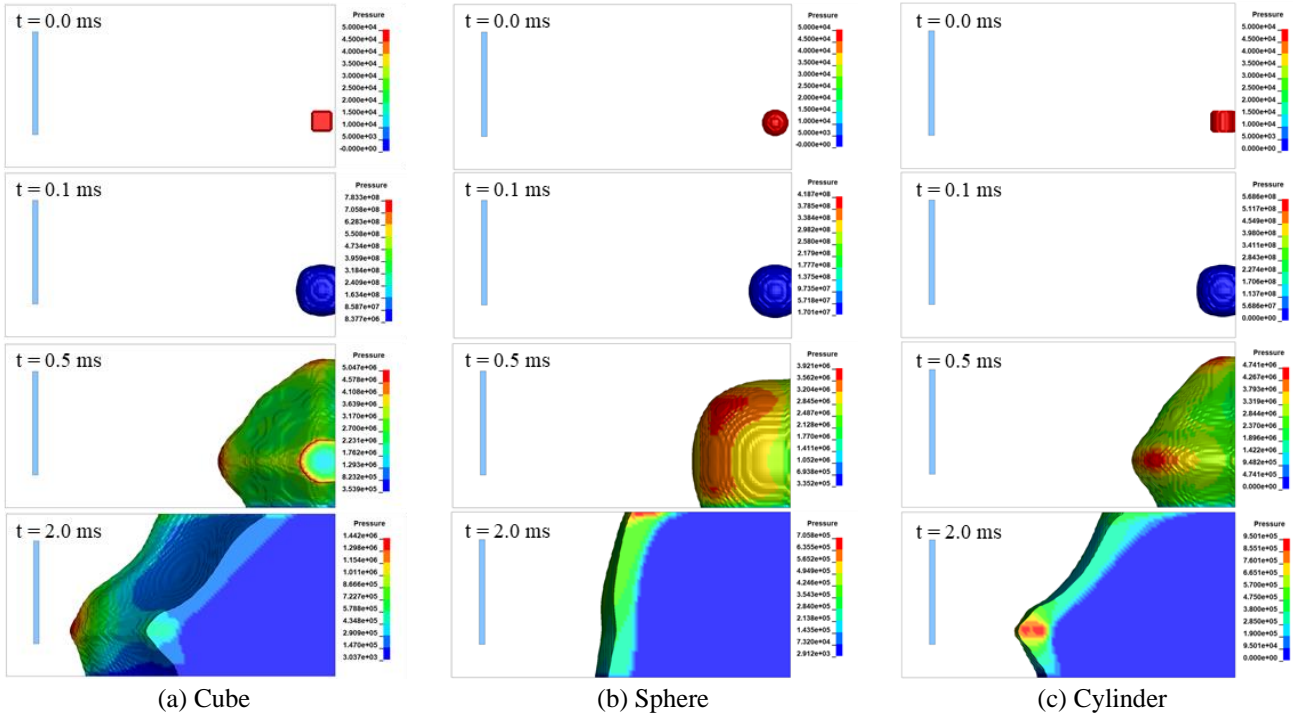


Fig. 9 Blast wave propagation according to the explosive type

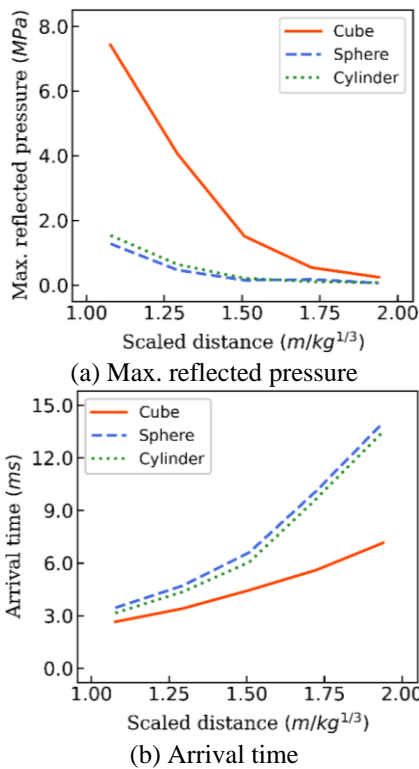


Fig. 10 Maximum reflected pressure and arrival time for different scaled distances

of a four-point bending test.

(2) Both the experimental and numerical results showed that HPCRCC slabs have better blast resistance compared to the RC slab with normal compressive strength. The superior blast-resistant performance is not only ascribed to the properties of the material itself, but

also to the important role that the confinement effect of the BFRP sheet used in KNU-HPFRCC plays in reducing destruction. Through a parametric study, it was found that there was not a significant difference in the performance of the HPFRCCs with a compressive strength over 100 MPa, but the thickness of the slab greatly affected the serviceability of the structure.

(3) Unlike the LBE method in which the blast pressure is obtained from the empirical equation, the ALE method can simulate the blast pressure considering the shape of the explosive and ground reflection. The reflected pressure at the short-scaled distance highly depends on the shape of explosive, while the effect of the shape of explosive on the arrival time increases at relatively long-scaled distance. From these results, accuracy and efficiency of the blast simulation can be achieved by adopting the appropriate numerical method for a given explosion condition.

### Acknowledgments

This research was supported by the Basic Science Research Program through the National Research Foundation of Korea (NRF) funded by the Ministry of Education (No. 2021R1A6A3A01088355) and was also supported by the National Research Foundation of Korea (NRF) grant funded by the Korea government (MSIT) (No. 2023R1A2C2005101).

### References

Department of Defense (DOD) (2008), Unified Facilities Criteria

- (UFC) Structures to Resist the Effects of Accidental Explosions, Department of Defense, Washington, D.C., USA.
- Baggio, D., Soudki, K. and Noel, M. (2014), "Strengthening of shear critical RC beams with various FRP systems", *Constr. Build. Mater.*, **66**, 634-644. <https://doi.org/10.1016/j.conbuildmat.2014.05.097>.
- Chen, W., Pham, T.M., Elchalakani, M., Li, H., Hao, H. and Chen, L. (2020), "Experimental and numerical study of basalt FRP strip strengthened RC slabs under impact loads", *Int. J. Struct. Stab. Dyn.*, **20**(6), 1-24. <https://doi.org/10.1142/S0219455420400015>.
- Chen, W., Pham, T.M., Sicheembe, H., Chen, L. and Hao, H. (2018), "Experimental study of flexural behaviour of RC beams strengthened by longitudinal and U-shaped basalt FRP sheet", *Compos. Part B: Eng.*, **134**, 114-126. <https://doi.org/10.1016/j.compositesb.2017.09.053>.
- Cui, J., Hao, H. and Shi, Y. (2017), "Discussion on the suitability of concrete constitutive models for high-rate response predictions of RC structures", *Int. J. Impact Eng.*, **106**, 202-216. <https://doi.org/10.1016/j.ijimpeng.2017.04.003>.
- Dhand, V., Mittal, G., Rhee, K.Y., Park, S.J. and Hui, D. (2015), "A short review on basalt fiber reinforced polymer composites", *Compos. Part B: Eng.*, **73**, 166-180. <https://doi.org/10.1016/j.compositesb.2014.12.011>.
- Gan, L., Zong, Z., Chen, Z., Wu, T., Lin, J. and Li, M. (2023), "Differences in responses of square steel plates exposed to blast loads generated by cubic and spherical explosives", *Thin Wall. Struct.*, **182**, 110332. <https://doi.org/10.1016/j.tws.2022.110332>.
- Jung, H., Park, S., Kim, S. and Park, C. (2017), "Performance of SIFCON based HPRCC under field blast load", *Proc. Eng.*, **210**, 401-408. <https://doi.org/10.1016/j.proeng.2017.11.094>.
- Kim, J., Lee, J., Jung, W. and Han, D. (2022), "Testing the anti-explosion protection of HPRCC for ready-mixed concrete system based on fiber selection and resistance to live explosives", *Case Stud. Constr. Mater.*, **17**, e01249. <https://doi.org/10.1016/j.cscm.2022.e01249>.
- Korea Institute of Civil Engineering and Building Technology (KICT), (2017), "Developments of impact/blast resistant HPRCC and evaluation techniques thereof (Final report in Korean)", Infrastructure R&D Report 18SCIPB128706-02; Korea Institute of Civil Engineering and Building Technology (KICT), Gyeonggi-do, Korea.
- KS F 2566. (2014), Standard Test Method for Flexural Performance of Fiber Reinforced Concrete, Korean Standards Association, Seoul, Korea.
- Kumar, V., Kartik, K.V. and Iqbal, M.A. (2020), "Experimental and numerical investigation of reinforced concrete slabs under blast loading", *Eng. Struct.*, **206**, 110125. <https://doi.org/10.1016/j.engstruct.2019.110125>.
- Lee, M.J., Kwak, H.G. and Park, G.K. (2021), "An improved calibration method of the K&C model for modeling steel-fiber reinforced concrete", *Compos. Struct.*, **269**, 114010. <https://doi.org/10.1016/j.compstruct.2021.114010>.
- Lee, M.J., Park, G.K., Kim, S.W. and Kwak, H.G. (2022), "Damage characteristics of high-performance fiber-reinforced cement composites panels subjected to projectile impact", *Int. J. Mech. Sci.*, **214**, 106919. <https://doi.org/10.1016/j.ijmecsci.2021.106919>.
- Li, Z., Chen, L., Fang, Q., Chen, W., Hao, H. and Zhang, Y. (2017), "Experimental and numerical study of basalt fiber reinforced polymer strip strengthened autoclaved aerated concrete masonry walls under vented gas explosions", *Eng. Struct.*, **152**, 901-919. <https://doi.org/10.1016/j.engstruct.2017.09.055>.
- Liu, J., Li, J., Fang, J., Liu, K., Su, Y. and Wu, C. (2022), "Investigation of ultra-high performance concrete slabs under contact explosions with a calibrated K&C model", *Eng. Struct.*, **255**, 113958. <https://doi.org/10.1016/j.engstruct.2022.113958>.
- Lu, D., Wang, G., Du, X. and Wang, Y. (2017), "A nonlinear dynamic uniaxial strength criterion that considers the ultimate dynamic strength of concrete", *Int. J. Impact Eng.*, **103**, 124-137. <https://doi.org/10.1016/j.ijimpeng.2017.01.011>.
- Luccioni, B., Isla, F., Codina, R., Ambrosini, D., Zerbino, R., Giaccio, G. and Torrijos, M.C. (2018), "Experimental and numerical analysis of blast response of high strength fiber reinforced concrete slabs", *Eng. Struct.*, **175**, 113-122. <https://doi.org/10.1016/j.engstruct.2018.08.016>.
- Park, J.K., Kim, S.W. and Kim, D.J. (2017), "Matrix-strength-dependent strain-rate sensitivity of strain-hardening fiber-reinforced cementitious composites under tensile impact", *Compos. Struct.*, **162**, 313-324. <https://doi.org/10.1016/j.compstruct.2016.12.022>.
- Ren, G.M., Wu, H., Fang, Q. and Liu, J.Z. (2018), "Effects of steel fiber content and type on static mechanical properties of UHPCC", *Constr. Build. Mater.*, **163**, 826-839. <https://doi.org/10.1016/j.conbuildmat.2017.12.184>.
- Shi, Y., Wang, N., Cui, J., Li, C. and Zhang, X. (2022), "Experimental and numerical investigation of charge shape effect on blast load induced by near-field explosions", *Pr. Saf. Environ. Protect.*, **165**, 266-277. <https://doi.org/10.1016/j.psep.2022.07.018>.
- Su, Q., Wu, H., Sun, H.S. and Fang, Q. (2021), "Experimental and numerical studies on dynamic behavior of reinforced UHPC panel under medium-range explosions", *Int. J. Impact Eng.*, **148**, 103761. <https://doi.org/10.1016/j.ijimpeng.2020.103761>.
- Tufekci, M.M. and Gokce, A. (2017), "Development of heavyweight high performance fiber reinforced cementitious composites (HPRCC) - Part I: Mechanical properties", *Constr. Build. Mater.*, **148**, 559-570. <https://doi.org/10.1016/j.conbuildmat.2017.05.009>.
- Wu, C., Fattori, G., Whittaker, A. and Oehlers, D.J. (2010), "Investigation of air-blast effects from spherical-and cylindrical-shaped charges", *Int. J. Protect. Struct.*, **1**(3), 345-362. <https://doi.org/10.1260/2041-4196.1.3.345>.
- Xu, J., Wu, C., Xiang, H., Su, Y., Li, Z. X., Fang, Q. and Li, J. (2016), "Behaviour of ultra high performance fibre reinforced concrete columns subjected to blast loading", *Eng. Struct.*, **118**, 97-107. <https://doi.org/10.1016/j.engstruct.2016.03.048>.
- Yoo, D.Y., Kim, S.W. and Park, J.J. (2017), "Comparative flexural behavior of ultra-high-performance concrete reinforced with hybrid straight steel fibers", *Constr. Build. Mater.*, **132**, 219-229. <https://doi.org/10.1016/j.conbuildmat.2016.11.104>.
- Zhang, F., Shedbale, A.S., Zhong, R., Poh, L.H. and Zhang, M.H. (2021), "Ultra-high performance concrete subjected to high-velocity projectile impact: Implementation of K&C model with consideration of failure surfaces and dynamic increase factors", *Int. J. Impact Eng.*, **155**, 103907. <https://doi.org/10.1016/j.ijimpeng.2021.103907>.

HK